# nature nanotechnology

**Article** 

https://doi.org/10.1038/s41565-022-01306-x

# Photocarrier-induced persistent structural polarization in soft-lattice lead halide perovskites

Received: 19 May 2022

Accepted: 24 November 2022

Published online: 26 January 2023



Qi Qian ® <sup>1,8</sup>, Zhong Wan ® <sup>1,8</sup>, Hiroyuki Takenaka<sup>2,8,9</sup>, Jong K. Keum ® <sup>3</sup>, Tyler J. Smart<sup>4,5</sup>, Laiyuan Wang ® <sup>1</sup>, Peiqi Wang ¹, Jingyuan Zhou¹, Huaying Ren ® ¹, Dong Xu<sup>6</sup>, Yu Huang ® <sup>6,7</sup>, Yuan Ping ® <sup>2</sup> ⋈ & Xiangfeng Duan ® <sup>1,7</sup> ⋈

The success of the lead halide perovskites in diverse optoelectronics has motivated considerable interest in their fundamental photocarrier dynamics. Here we report the discovery of photocarrier-induced persistent structural polarization and local ferroelectricity in lead halide perovskites. Photoconductance studies of thin-film single-crystal CsPbBr<sub>3</sub> at 10 K reveal long-lasting persistent photoconductance with an ultralong photocarrier lifetime beyond 10<sup>6</sup> s. X-ray diffraction studies reveal that photocarrier-induced structural polarization is present up to a critical freezing temperature. Photocapacitance studies at cryogenic temperatures further demonstrate a systematic local phase transition from linear dielectric to paraelectric and relaxor ferroelectric under increasing illumination. Our theoretical investigations highlight the critical role of photocarrier-phonon coupling and large polaron formation in driving the local relaxor ferroelectric phase transition. Our findings show that this photocarrier-induced persistent structural polarization enables the formation of ferroelectric nanodomains at low temperature, which suppress carrier recombination and offer the possibility of exploring intriguing carrier-phonon interplay and the rich polaron photophysics.

Soft-lattice lead halide perovskites (LHPs) exhibit remarkable photocarrier properties, such as low carrier recombination rates, high carrier mobilities and long charge diffusion lengths<sup>1,2</sup>, in addition to many other intriguing phenomena that include slow hot carrier cooling<sup>3</sup>, quantum interference<sup>4</sup> and giant spin-orbit coupling<sup>5,6</sup>. Along with low-cost solution processability and unusual defect tolerance<sup>7,8</sup>, these extraordinary characteristics make LHPs an attractive material system for optoelectronics

and spintronics as well as an exciting material platform for fundamental studies.

However, despite the tremendous success in proof-of-concept devices including photovoltaics and light-emitting diodes <sup>9,10</sup>, the fundamental origins of these properties are not entirely clear. Among many theories proposed for their carrier recombination and transport properties, the concept of large polarons<sup>11</sup> is of particular interest. In this picture, the excess electrons or holes in such soft-lattice

<sup>1</sup>Department of Chemistry and Biochemistry, University of California, Los Angeles, CA, USA. <sup>2</sup>Department of Chemistry and Biochemistry, University of California Santa Cruz, Santa Cruz, CA, USA. <sup>3</sup>Center for Nanophase Materials Science and Neutron Scattering Division, Oak Ridge National Laboratory, Oak Ridge, TN, USA. <sup>4</sup>Department of Physics, University of California Santa Cruz, Santa Cruz, CA, USA. <sup>5</sup>Lawrence Livermore National Laboratory, Livermore, CA, USA. <sup>6</sup>Department of Materials Science and Engineering, University of California, Los Angeles, CA, USA. <sup>7</sup>California NanoSystems Institute, University of California, Los Angeles, CA, USA. <sup>8</sup>These authors contributed equally: Qi Qian, Zhong Wan, Hiroyuki Takenaka. <sup>9</sup>Deceased: Hiroyuki Takenaka. <sup>∞</sup>e-mail: yuanping@ucsc.edu; xduan@chem.ucla.edu

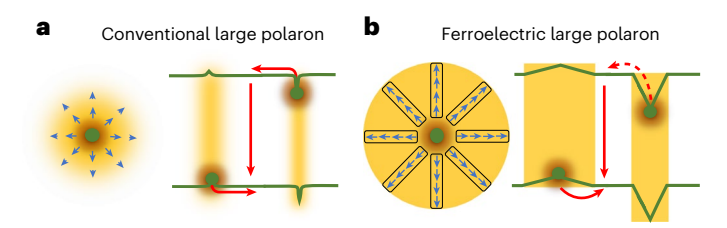


**Fig. 1** | **Difference between conventional and ferroelectric large polarons. a**, Left: a conventional large polaron in which the dipole moment in a unit cell (blue arrow) in the presence of an extra charge (green sphere) decays rapidly with increasing distance from the charge. Right: schematic potential profile for the conventional large polaron, which deceases rapidly with distance away from the charge. **b**, Left: a ferroelectric large polaron in which the dipole moments in a polar nanodomain are uniformly affected by the charge. Right: schematic potential profile for the ferroelectric large polaron, showing a linear decrease with distance away from the charge, with a much wider and deeper potential well than in the conventional large polaron. The shaded area highlights the region of dipole formation, and the red lines represent the recombination paths, with solid and dashed lines representing large and small probability events, respectively. The potential well for the electron polaron is deeper and narrower compared with the hole polaron. Only hole polarons are plotted as examples in the left-side schematics.

materials induce local lattice distortions that extend over multiple unit cells, forming large polarons (Fig. 1a, left)<sup>3,11,12</sup>. The formation of large polarons under photoexcitation physically separates the electrons and holes (Fig. 1a, right), leading to a long carrier lifetime and an enhanced photovoltaic performance. Indeed, several pioneering studies have revealed signatures of large polaron formation in LHPs from the interpretation of hot carrier lifetimes<sup>3,11</sup>, mobility/density characteristics<sup>4,13</sup>, large hole effective masses<sup>14</sup> and polaron-induced strain fields<sup>15</sup>.

The contribution of ferroelectricity to the charge carrier recombination in LHPs has also been proposed<sup>16-18</sup>, where electrons and holes travel in distinct paths along ferroelectric domains, reducing the recombination probability, although the exact origin remains to be fully resolved 19-22. It has also been suggested that polaron formation and the associated lattice distortions may lead to a net accumulation of charge dipole momentum and the construction of a ferroelectric domain with a robust uniform polarization within the domain, regardless of the distance from the charge centre, forming 'ferroelectric large polarons' (Fig. 1b, left)<sup>23,24</sup>. Such ferroelectric polarization could result in the electron and hole polarization domains with much wider and deeper potential wells (Fig. 1b, right)<sup>11,16,25,26</sup>, further reducing the probability of charge recombination<sup>23,24</sup>, leading to an even longer carrier lifetime. However, a direct evaluation of ferroelectric behaviour in LHPs and its correlation with charge carrier recombination<sup>23</sup> or photocarrier transport properties has been elusive, partly due to the complication from considerable ionic movement or irreversible photochemical processes at room temperature or during thermal cycling studies. A systematic photocarrier transport study at cryogenic temperatures can largely avoid such complications, but has been challenging due to the difficulties in making reliable contacts that can survive cryogenic transport or thermal cycling studies.

Here we use a highly robust van der Waals contact approach to conduct systematic photocarrier transport studies at cryogenic temperatures and report the discovery of a long-lasting persistent photoconductance in thin-film CsPbBr<sub>3</sub> with a persistent photocarrier density of  $10^{15}$ – $10^{16}$  cm<sup>-3</sup> and a lifetime of  $1.0 \times 10^6$  s at low temperature (<20 K). Our X-ray diffraction studies directly confirm the photocarrier-induced structural distortion, which is persistent at cryogenic temperature but vanishes upon warming beyond a critical freezing temperature (-100 K). Photocapacitance studies confirm a local phase transition from linear dielectric to paraelectric and relaxor

ferroelectric upon photoillumination. Theoretical investigations further highlight the important role of photocarrier-driven structural distortion to the observed local relaxor ferroelectric phase. Together, our study provides robust evidence of photocarrier-induced structural polarization and ferroelectric large polarons in CsPbBr $_3$ , which are persistent below a critical freezing temperature without continued photoexcitation and vanish upon warming and removal of the persistent photocarriers.

#### Persistent photoconductance

The CsPbBr<sub>3</sub> thin film was grown on a muscovite substrate using a home-built chemical vapour deposition system. All devices used in this study were fabricated through a van der Waals integration process to avoid undesired material degradation of the delicate perovskites and ensure robust contact that can survive measurements at cryogenic temperatures<sup>4,27</sup>. We first conducted electrical transport studies based on a standard Hall bar device (see Methods for details). In general, the transport is dominated by holes. Before illumination, the CsPbBr<sub>3</sub> film shows a rather low conductance (G) of  $\sim 3.1 \times 10^{-10}$  S at 10 K (Fig. 2a,b). Upon a photoillumination at 18.8 mW cm<sup>-2</sup>, the conductance instantly increases by four orders of magnitude to  $3.0 \times 10^{-6}$  S as a result of photocarrier generation. After turning off the light illumination, the conductance exhibits a rapid decrease but does not go back to the original conductance under the dark condition, and instead shows a persistent photoconductance much higher than that measured before illumination, without any apparent sign of decay for over  $7.0 \times 10^4$  s. The instant reduction in the photoconductance immediately after termination of the illumination is attributed to the commonly observed recombination of free photocarriers (with a lifetime in the range of microseconds to milliseconds), and the remanent persistent photoconductance is the focus of our current study. Such a persistent photoconductance indicates the presence of very long-lasting photocarriers. Exponential fitting of the decay profile of the persistent photoconductance reveals a persistent photocarrier lifetime  $\tau$  of up to 1.0 × 10<sup>6</sup> s at 10 K (Fig. 2c, blue; see also Methods for details). With increasing temperature T, the persistent photoconductance decreases much more quickly, leading to a rapidly decreasing persistent photocarrier lifetime (for example,  $7.8 \times 10^2$  s at 200 K; see Fig. 2c,d and Supplementary Fig. 1).

The overall  $G_{\rm light}$  increases with the illumination power density, whereas the persistent photoconductance starts to saturate at 18.8 mW cm<sup>-2</sup> (Fig. 2e,f). At 10 K, the intrinsic carrier (hole) density under the original dark conditions is <9.3 ×  $10^{12}$  cm<sup>-3</sup>; by contrast, that under a steady-state illumination of 18.8 mW cm<sup>-2</sup> is  $4.6 \times 10^{16}$  cm<sup>-3</sup> and the remanent carrier density under the persistent photoconductance condition (that is, dark after 18.8 mW cm<sup>-2</sup> illumination) is  $8.2 \times 10^{15}$  cm<sup>-3</sup> (Supplementary Table 1). In this regard, ~20% of the steady-state carriers are the result of those with a much longer lifetime. The saturation of persistent carriers at a density of  $8.2 \times 10^{15}$  cm<sup>-3</sup> suggests a minimum separation of ~30 nm is needed for the persistent carriers, and below this distance, their wavefunctions start to overlap and recombination occurs.

# Photocarrier-induced persistent structural polarization

We note that conventional trapping states could be a trivial explanation for the apparently long-lived photocarriers. To this end, we measured the trap density using the space-charge-limited current (or SCLC) model at 10 K (Supplementary Fig. 2), which gave a trap density of  $1.0 \times 10^{14}$  cm<sup>-3</sup>, nearly two orders of magnitude lower than the observed persistent photoconductance carrier density ( $8.2 \times 10^{15}$  cm<sup>-3</sup>). Thus, the conventional trap states are present at too low a density to be responsible for the notable persistent photoconductance observed in our study. We also note that ion movement could be a possible contributor. Earlier studies of the ionic conductivity in LHPs gave an activation energy  $E_{\rm ion}$  of >150 meV (refs.  $^{28-30}$ ), which is much greater than the temperature

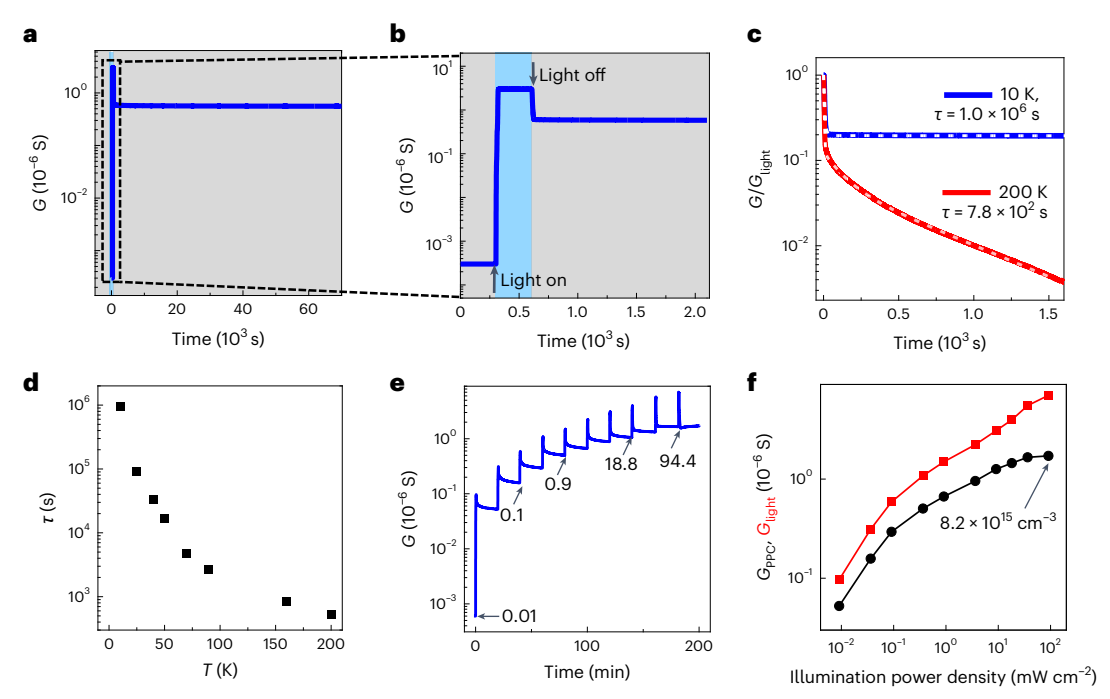


**Fig. 2** | **The long-lived photocarriers. a,b**, Long-lasting persistent photoconductance that shows no apparent sign of decay during the measurement timescale (**a**), and expanded version of the initial 2,000 s, with the arrows highlighting the light-on and light-off events (**b**). The blue and grey shaded areas correspond to the light-on and -off regions, respectively. **c**, Persistent photoconductance at 200 K compared with that at 10 K, where the conductance G is normalized by the conductance under illumination  $G_{\text{light}}$ . The persistent photocarrier lifetime  $\tau$  at 10 K and 200 K is  $1.0 \times 10^6$  s and  $7.8 \times 10^2$  s,

respectively. The dashed lines show fits to the photoconductance decay at each temperature.  $\mathbf{d}$ , Temperature dependence of the persistent photocarrier lifetime  $\mathbf{r}$ . The illumination power used here is 18.8 mW cm<sup>-2</sup>.  $\mathbf{e}$ , Illumination-dependent persistent photoconductance. The illumination was turned on and off in steps at 20 min intervals, and the illumination power values in the plot have units of mW cm<sup>-2</sup>.  $\mathbf{f}$ , Conductance under illumination ( $G_{\text{light}}$ , red) and persistent photoconduce ( $G_{\text{PPC}}$ , black) measured at the end of each time interval plotted as a function of the illumination power density.

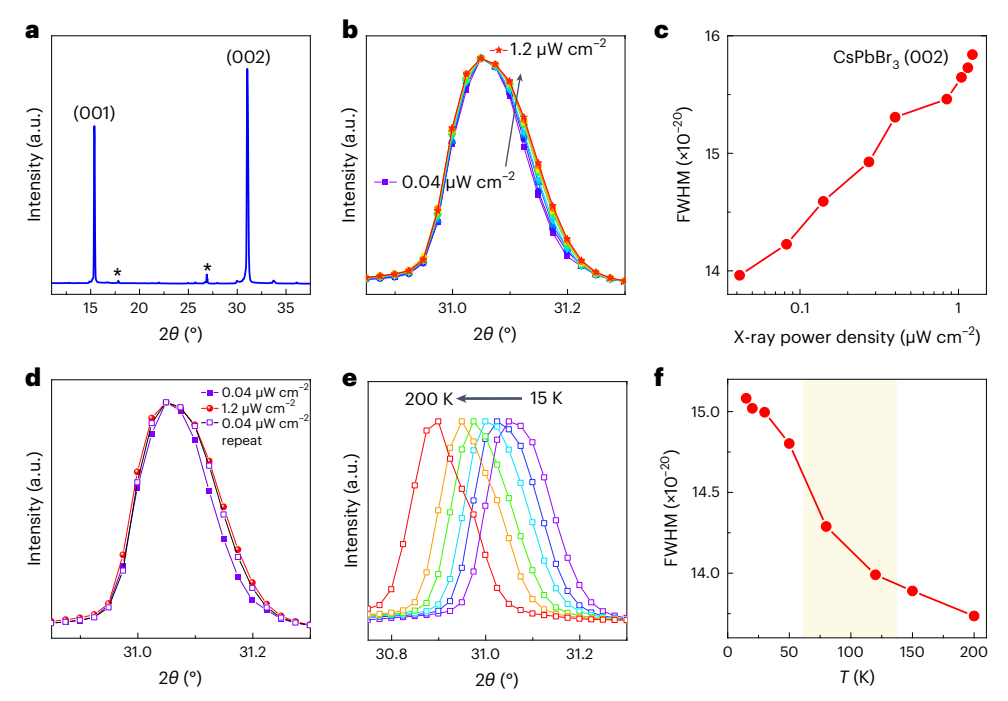
regime of our study. In general, the ion movement is completely frozen out below 200 K (ref.  $^4$ ). In addition, thermal cycling studies show that the persistent photoconductance effect decreases with increasing temperature and vanishes completely when the system warms beyond a critical temperature (75–150 K) (Supplementary Fig. 3), indicating that persistent photoconductance is not the result of any irreversible structural change or photochemical modifications.

Since neither conventional traps, ionic movement nor photochemical doping can satisfactorily explain our observed persistent photoconductance, we invoked a ferroelectric large polaron picture (Fig. 1b)<sup>23,24</sup>. To this end, we carried out X-ray diffraction structural analysis under different X-ray illumination intensities at low temperature (15 K). It has been shown previously that X-ray illumination can generate charge carriers in LHPs<sup>31,32</sup>. Thus, a systematic variation of the X-ray intensity can have a similar effect as photoillumination in producing variable photocarrier density (Methods). Overall, the X-ray diffraction patterns show the (00*l*) family planes of CsPbBr<sub>3</sub> (Fig. 3a). Interestingly, a close examination of the (002) peak reveals a notable peak broadening with increasing X-ray intensity (Fig. 3b). The full-width at half-maximum (FWHM) increases monotonically with the X-ray power density (Fig. 3c), directly confirming the photocarrier-induced lattice distortion. Moreover, we noticed that the broadening of the X-ray diffraction peak is more dominated by the higher angle side with a smaller lattice spacing (Fig. 3b), consistent with previous theories about the hole-polaron-dominated scenario 33,34 in which the formation of hole polarons leads to shrinking of the lattice spacing. The more dominant role of hole polarons is also consistent with hole-dominated transport characteristics 4,35,36.

Such notable peak broadening is persistent at low temperature: it does not go back to that seen under the low-power condition after illumination at a high X-ray power density (Fig. 3d). On the other hand,

temperature-dependent studies show that such a persistent structural change developed at low temperature vanishes upon warming, with an apparent transition region around 75–150 K or so (Fig. 3e,f), which is highly correlated with the disappearance of the persistent photoconductance in this temperature regime (Supplementary Fig. 3). Similar behaviour is also seen in the CsPbBr $_3$  (001) peak (Supplementary Fig. 4) but not in the diffraction peaks of the mica substrate (Supplementary Fig. 5), indicating that the peak broadening or structural distortion is unique to CsPbBr $_3$ .

We note that the photochemical doping or photoactivation of conventional traps in LHPs may also lead to possible structural change. Such change is usually limited to the atomic or individual lattice level. Considering that a photocarrier density of 10<sup>15</sup> cm<sup>-3</sup> (in our X-ray excitation range; see also Methods) corresponds to a charge separation of 100 nm, if the structural change is limited to individual lattice or small polarons (<1 nm), the overall volume that may show any structural change is expected to be <0.001%, which is not typically detectable via X-ray diffraction studies. The fact that we observed a notable structural change at such a low carrier density (1015 cm<sup>-3</sup>) clearly indicates a long-range polarization effect (of the order of 10 nm or larger, that is, large polarons). In addition, the structural change induced by photochemically generated impurities or defect states is normally expected to be irreversible, whereas that induced by polaron states could lead to highly reversible lattice distortion once the carriers are removed. Together, this persistent and reversible structural change, which is directly correlated with the generation of persistent photocarriers at low temperature and vanishes above a certain critical freezing temperature, strongly supports the formation of persistent polaron states (that is, ferroelectric large polarons) in which the collectively polarized nanodomains physically separate the electrons and holes, producing a potential barrier against charge recombination.



 $\label{eq:fig.3} Photocarrier-induced structural distortion. a, X-ray diffraction pattern of the $C$PbBr_3$ thin film shows only (00$ *l* $) family planes. Peaks from the monoclinic phase of the muscovite substrate are marked with an asterisk. The measurements were conducted under an X-ray power density of <math>1.2~\mu W~cm^{-2}$  at 15~K. b, Normalized X-ray diffraction data obtained around the \$C\$PbBr\_3\$ (002) peak with different X-ray power densities at 15~K, showing the apparent broadening towards the higher diffraction angle with an increasing X-ray power density and indicating more local lattice distortion with increasing charge carrier generation. c, FWHM plotted as a function of the X-ray power density for the \$C\$PbBr\_3\$ (002) peak. d, Persistent X-ray diffraction (002) peak broadening

observed in CsPbBr $_3$  at 15 K. e, Temperature-dependent CsPbBr $_3$  (002) peak measured under an X-ray power density of 0.04  $\mu$ W cm $^{-2}$  after high-flux irradiation at 1.2  $\mu$ W cm $^{-2}$  show persistent peak broadening at low temperature, which starts to narrow upon warming beyond 75–150 K or so. f, FWHM of the CsPbBr $_3$  (002) peak plotted as a function of temperature. The shaded area highlights the regions where the broadening decreases, corresponding to the thermally activated region in the transport studies. We note that the decrease in FWHM upon heating is not simply because the slight diffraction angle shifts to a smaller value (that is, thermal expansion). Such a shift would result in a much smaller FWHM difference.

# Photocarrier-induced local polar phase

We further carried out photocapacitance measurements in a frequency range from 1 kHz to 1 MHz to study the dielectric and ferroelectric properties. The device used for such studies consisted of a peeled CsPbBr<sub>3</sub> perovskite thin film sandwiched between two Au electrodes (Fig. 4a). The relative dielectric constant ( $\varepsilon'$ ) measured under dark conditions remained nearly constant from 300 to 4 K and decreased with increasing excitation frequency (Fig. 4b). The  $\varepsilon'$  value under dark conditions is around 20-26 and is largely consistent with those reported previously<sup>37,38</sup>. However, when using a relatively low illumination of 0.1 mW cm<sup>-2</sup>, the temperature-dependent  $\varepsilon'$  exhibits a notable peak, with a value of 68 at 63 K under an excitation frequency of 1 MHz (Fig. 4c). This behaviour resembles typical ferroelectric materials, in which a dielectric peak develops at the ferroelectric transition temperature<sup>39</sup>. Our measurements at different excitation frequencies show that the dielectric constant peak shifts towards a lower temperature with a decreasing measurement frequency. The frequency dependence of these  $\varepsilon'$ -T curves is a strong indicator of the relaxor ferroelectric phase, which is distinct from a normal ferroelectric material in which the peak position of the  $\varepsilon'$ -T curve does not vary with excitation frequency<sup>39</sup>, as is usually observed in hybrid LHPs 40,41.

Such a dispersion of the dielectric constant is the signature of a broad distribution of relaxation times with a characteristic relaxation time  $\tau_c$  (defined by the excitation frequency f in  $\frac{1}{2\pi f}$ ) and is expected to obey the Vögel–Fulcher relationship  $^{42,43}$ :

$$\tau_{\rm c} = \frac{1}{2\pi f} = \tau_{\rm c0} \exp\left(\frac{\Delta E_{\rm VF}}{T_{\rm M} - T_{\rm F}}\right) \tag{1}$$

where  $\tau_{c0}$  is the microscopic attempt time and  $\Delta E_{VF}$  is the average energy barrier, which can be viewed as the average energy for the charge dipole depolarization. In addition,  $T_{\rm M}$  is the temperature at which  $\varepsilon'$  reaches its maximum value and  $T_{\rm F}$  is the freezing temperature, towards which the freezing phenomenon takes place in the material when the temperature decreases. Indeed, the plot of  $\tau_{\rm c}$  as a function of  $T_{\rm M}$  can be well fitted using equation (1) (Fig. 4d), giving a freezing temperature  $T_{\rm F}$  of 22 K and an average energy barrier  $\Delta E_{\rm VF}$  of 13 meV.

Next, we systematically investigated the illumination-powerdependent  $\mathcal{E}'$ , extracting  $\Delta E_{\text{VF}}$  and  $T_{\text{F}}$  for different illumination intensities (Supplementary Figs. 6 and 7). Both  $\Delta E_{VF}$  and  $T_{F}$  show a monotonic increase with the illumination power density (Fig. 4e), highlighting that with more photocarriers, more local distortions are triggered, leading to a more robust relaxor phase. The capacitance–electric field (*C–E*) curve measured in the dark at 5 K shows no response to the external electric field (Fig. 4f, black), and the polarization-electric field (P-E) curve shows a perfect linear relationship with the electric field (Fig. 4g, black), which is consistent with the expected behaviour of linear dielectric materials. By contrast, under 0.01 mW cm<sup>-2</sup> light illumination, a peak was observed in the C-E profile but with little hysteresis between the forward and backward scans (Fig. 4f, red). The corresponding P-E curve shows the highest slope near zero electric field with a reduced slope at higher field (Fig. 4g, red). Such behaviour is consistent with the picture of paraelectric materials, where the electric dipoles exist but have not yet started to form any domain. When the illumination intensity is increased further to ≥0.1 mW cm<sup>-2</sup>, clear hysteresis emerges in the C-E and P-E data (Fig. 4f,g, respectively, and Supplementary Fig. 8a,b, respectively).

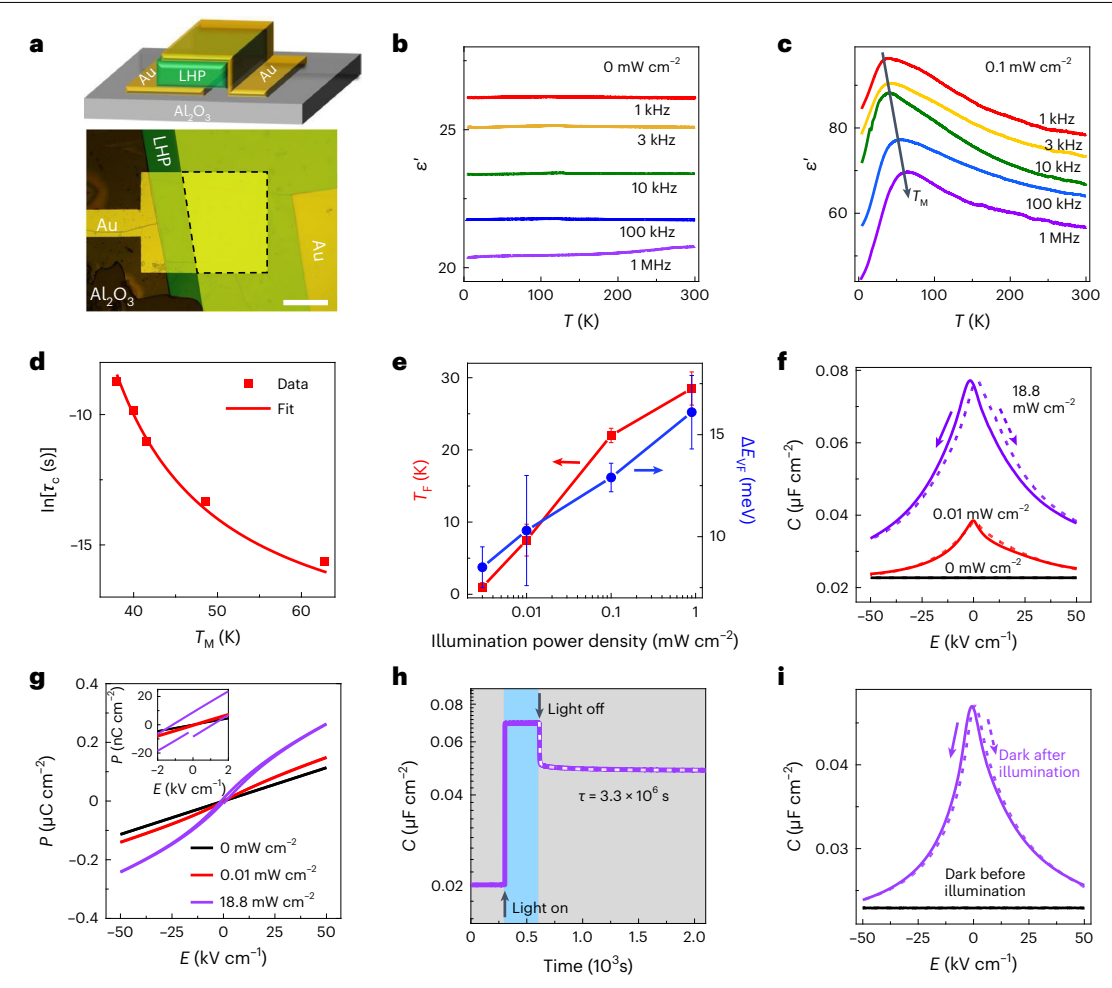


**Fig. 4** | **Emergence of local relaxor ferroelectric behaviour under illumination. a**, The schematic layout (top) and false-coloured microscope image (bottom) of a typical device for photocapacitance measurements. Scale bar, 200 μm. **b**, Temperature-dependent dielectric constant  $\varepsilon'$  measured without illumination in the frequency range from 1 kHz to 1 MHz, which shows no apparent change with temperature. **c**, Temperature-dependent dielectric constant  $\varepsilon'$  measured at an illumination intensity of 0.1 mW cm<sup>-2</sup>, showing behaviour typical of the paraelectric to relaxor ferroelectric phase transition. The arrow is a guide to the eye that highlights the shift in the temperature of the  $\varepsilon'$  peak maximum ( $T_{\rm M}$ ) with the excitation frequency. **d**, Relaxation time  $T_{\rm c} = (2\pi f)^{-1}$  versus  $T_{\rm M}$  and the fit to the Vögel–Fulcher relationship, which yields a freezing temperature ( $T_{\rm F}$ ) of 22 K and an energy barrier ( $\Delta E_{\rm VF}$ ) of 13 meV. **e**, The dependence of  $\Delta E_{\rm VF}$  (blue) and  $T_{\rm F}$  (red) on the illumination power density. The error bars are from the Vögel–Fulcher relationship fitting uncertainties. **f**, **g**, Plots of capacitance (C) versus electric field (E) (**f**) and polarization (P) versus E (**g**)

measured at a 1 MHz excitation frequency under different illumination intensities at 5 K. With increasing illumination intensity, the system evolves from a linear dielectric (black) to paraelectric (red) to relaxor ferroelectric (purple) phase. The dashed (solid) lines in **f** show electric field scans from negative (positive) to positive (negative) fields. Inset: the expanded plot around zero electric field. We note that there is some minor discontinuity at E = 0 in the P - E loop, which is due to the slight asymmetry of the top and bottom contacts. **h**, The very long-lasting persistent photocapacitance at 5 K, which shows an exceptionally long carrier lifetime  $\tau$  of  $3.3 \times 10^6$  s, consistent with persistent photoconductance studies. The blue and grey shaded areas correspond to the light-on and -off regions, respectively. The dashed lines show fits to the photocapacitance decay. **i**, C - E data measured in the dark before illumination (black) and in the dark after illumination (purple) at 5 K. The dashed (solid) lines show electric field scans from negative (positive) to positive (negative) fields.

The  $\operatorname{slim} P - E \operatorname{loop}$  and the relatively small remanent polarization  $P_R$  (Supplementary Fig. 8c) suggest that, without applying an external electric field, the polarization integrated over all polar nanodomains effectively cancel each other out, leaving a very small net polarization. This is consistent with the ferroelectric large polaron picture in Fig. 1b, in which the ideal overall polarization for each ferroelectric large polaron should be zero in the absence of an external electric field. We should note that the ferroelectricity observed here is not a macroscopic phenomenon but develops as individual polarons show ferroelectric characteristics, as also described in the recent perspective of Miyata and Zhu²³. In addition, a temperature-dependence study (Supplementary Fig. 8d,e) shows the disappearance of hysteresis at elevated temperatures, which excludes the effect of ion movement on the observed ferroelectricity because ion movement is expected to be more pronounced at higher temperature.

Similar to the persistent photoconductance discussed in Fig. 2, our system also shows persistent capacitance at 5 K with an exceptionally long persistent lifetime  $\tau$  of 3.3 × 106 s (Fig. 4h and Supplementary Fig. 9a). The corresponding  $\varepsilon'$  of >50 is maintained over the entire measurement duration after turning off the light (Supplementary Fig. 9b,c), which is considerably larger than the  $\varepsilon'$  value measured before illumination (that is, 20). The C-E trace measured after turning off the light illumination shows a clear peak and hysteresis near zero field (Fig. 4i), suggesting that the relaxor ferroelectric behaviour is retained with the persistently polarized nanodomains under dark conditions after illumination. This feature is clearly distinct from that measured before illumination and confirms the presence of very long-lasting persistent photocarriers, structural polarization and the associated ferroelectric nanodomains. In addition, the system reverts back to the linear dielectric phase through a cycle of warming and re-cooling in the dark

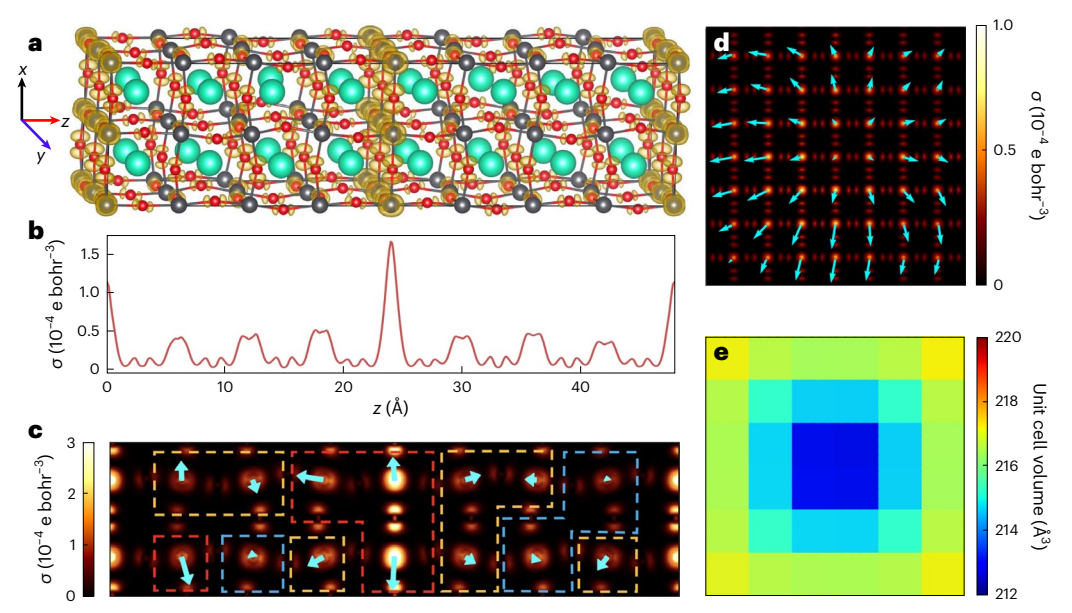


**Fig. 5** | **DFT calculations. a**, Lattice distortion and spin charge density distribution of the relaxed structures of a  $2 \times 2 \times 8$  CsPbBr<sub>3</sub> supercell with an extra hole. Green, Cs; grey, Pb; red, Br. The yellow colour represents the spin charge density, with a larger area showing a higher density. **b**, Averaged spin charge density  $\sigma$  in the x-y plane projected along the z axis. The most spin charge density is accumulated at the centre layer, consistent with the so-called pancake description of hole polarons in earlier work  $^{24,49}$ . **c**, Colour contour plot of spin charge density projected in the x-z plane and its correlation with the local polarization. Arrows located on Pb sites denote the local polarizations, with a longer arrow representing a larger polarization value. The red, orange and blue

dashed boxes denote polarization regions with  $|P| \ge 10$ ,  $10 > |P| \ge 5$  and |P| < 5 ( $\mu$ C cm $^{-2}$ ), respectively. **d**, Colour contour map of spin charge density and local polarization in the  $8 \times 8 \times 2$  supercell projected in the x-y plane. Arrows located on Pb sites denote the local polarizations, with a longer arrow representing a larger polarization value. **e**, The corresponding colour map of the volume of unit cell boxes defined by the eight corner Cs atoms. The green colour reflects the pristine unit cell volume of 216 Å $^3$ . We cut off the region near the top and right boundaries to shift the middle of Pb site to the centre in order to remove results at the artificial boundary.

(Supplementary Fig. 8f), during which the ferroelectric large polarons are annihilated, which indicates that the photoexcitation-induced ferroelectricity also does not originate from irreversible chemical segregation or photochemical doping.

The relaxor ferroelectricity discussed here is essentially different from the widely studied oxide perovskites that are typically characterized through chemical disorder  $^{44-47}$ , for example, the Ti content in the relaxor ferroelectric system PMN-PT  $^{47}$ . It is also different from recently discovered chain-chirality-triggered structure disorder in the relaxor ferroelectric copolymers P(VDF–TrFE) with different VDF contents (where P denotes poly, VDF is vinylidene fluoride and TrFE is trifluoroethylene)  $^{48}$ . The emergence of relaxor behaviour in photoexcited CsPbBr $_3$  is intriguing as it comes completely from photocarriers that drag the local lattice distortion (Fig. 3) to form polarons and modify the material polarizability, without changing the actual chemical content, thus highlighting the uniqueness of this material system.

### Theroretical investigations

We further performed density functional theory (DFT) calculations to explore how carrier–phonon coupling affects the local structure distortion and the ferroelectric polarization in CsPbBr $_3$ . To this end, we first fully relaxed the atomic positions in a  $2 \times 2 \times 8$  supercell with an excess charge and examined the spin charge density (charge density difference between up and down spin, which largely reflects the excess charge distribution). For simplicity here, we focus our discussion on hole polarons, and parallel results on electron polarons are presented in Supplementary Fig. 10. As a result of strong carrier–phonon coupling in this soft-lattice system, we see strongly distorted lattices in the presence of the excess holes (Fig. 5a). Interestingly, the high spin charge density appears mostly at the centre with some at the periodic boundary regions (Fig. 5a). This spin charge density at the boundary regions may be a result of the periodic boundary conditions enforced

by a finite box length and is thus not physically important. The averaged spin charge density of the x-y plane projected along the z axis clearly shows the highest spin charge density at the centre (Fig. 5b). This is consistent with the recently suggested 'pancake' or 'Belgian waffle' model for polarons in halide perovskites  $^{24,49}$ . The relaxed structure gives rise to highly polarized regions ( $|P| \ge 10~\mu C~cm^{-2}$ ) along with essentially negligible polarization regions ( $|P| \le 5~\mu C~cm^{-2}$ ; see also Fig. 5c). Comparing the polarization strength with the spin charge density, it is found that the area with a larger spin charge density typically shows stronger polarization, highlighting the important role of charge accumulation on the observed ferroelectric behaviour, consistent with the experimental observation shown in Fig. 4. The difference in the local polarization values indicates the coexistence of polar and non-polar regions and confirms the existence of the local relaxor phase in the intrinsically non-polar CsPbBr $_3$  upon the introduction of extra charge carriers.

Next, we further examined the spin charge density in the x-y plane of the central slice of the 2 × 2 × 8 supercell (Supplementary Fig. 11) and found that the overall spin charge distribution is largely constrained by the periodic boundary condition. We therefore further expanded the supercell size to  $8 \times 8 \times 2$  to weaken the boundary constraints in the x-y plane. When there is an extra hole, the spin charge density (brighter spot) shows a broad spread throughout the entire supercell with a gradual decay away from the charge centre (Fig. 5d), suggesting a rather delocalized hole state, thus forming a large polaron that is probably larger than the supercell size. By contrast, in the case of an excess electron, the spin charge density rapidly decays away from the charge centre, suggesting a more localized electron state (Supplementary Fig. 10d). This feature is consistent with previous experimental observations that more mobile holes dominate the electronic transport  $^{4,35,36}$ . The polarization strength (the arrow length in Fig. 5d) is strongly correlated with the spin charge density in this plane as well. Overall, the hole polaron exhibits an anisotropic local polarization pattern pointing

outwards from the centre with a swirl-like pattern (Fig. 5d), whereas the electron case features a symmetrically centripetal local polarization pattern (Supplementary Fig. 10d).

We examined the structural distortion and polaron formation further by evaluating the volumes of the unit cell boxes defined by the eight corner Cs atoms. Compared with the pristine unit cell volume of 216 Å<sup>3</sup>, the cell volume shrinks considerably near the hole-polaron centre, which gradually relaxes back towards the pristine value away from the charge centre (Fig. 5e). On the other hand, the cells near the electron-polaron centre show a slightly larger volume (Supplementary Fig. 10e). Overall, we see more notable cell shrinking in hole polarons and less cell expansion in electron polarons. This is consistent with the X-ray diffraction studies in Fig. 3b, where a more notable broadening to high-angle side (smaller cell size) is observed. It should be noted that DFT calculations for the 8 × 8 × 2 supercells in this study reach our computational limit, and we stress that developments in the methodology are necessary in future studies to investigate satisfactorily extended supercells with carrier-phonon coupling along all the Cartesian directions to diminish the periodic boundary condition effect.

#### Conclusion

In summary, the observation of photocarrier generation, photocarrierinduced local ferroelectric behaviour and photocarrier-induced lattice distortion (that is, polaron formation), which is persistent at low temperature and fully reversible upon thermal cycling, robustly demonstrates ferroelectric large polaron formation below a critical freezing temperature in a CsPbBr<sub>3</sub> thin film. In particular, the persistent and reversible photocarrier-induced structural distortion cannot be interpreted via conventional trapping states or irreversible photochemical modifications. The formation of ferroelectric nanodomains upon photoexcitation at low temperature produces a potential barrier against charge recombination and results in a very long-lasting persistent photoconductance and photocapacitance. Together, our results highlight soft-lattice LHPs as an exciting material platform for exploring the rich polaron photophysics and will inspire a new wave of interest in probing the intriguing interplay between soft-lattice dynamics and optoelectronic properties.

#### Online content

Any methods, additional references, Nature Portfolio reporting summaries, source data, extended data, supplementary information, acknowledgements, peer review information; details of author contributions and competing interests; and statements of data and code availability are available at https://doi.org/10.1038/s41565-022-01306-x.

#### References

- Stranks, S. D. et al. Electron-hole diffusion lengths exceeding 1micrometer in an organometal trihalide perovskite absorber. Science 342, 341–344 (2013).
- Herz, L. M. Charge-carrier mobilities in metal halide perovskites: fundamental mechanisms and limits. ACS Energy Lett. 2, 1539–1548 (2017).
- 3. Zhu, H., Miyata, K., Fu, Y., Wang, J. & Joshi, P. P. Screening in crystalline liquids protects energetic carriers in hybrid perovskites. *Science* **353**, 1409–1414 (2016).
- Wang, Y. et al. Probing photoelectrical transport in lead halide perovskites with van der Waals contacts. Nat. Nanotechnol. 15, 768–775 (2020).
- Niesner, D. et al. Giant Rashba splitting in CH<sub>3</sub>NH<sub>3</sub>PbBr<sub>3</sub> organicinorganic perovskite. *Phys. Rev. Lett.* 117, 126401 (2016).
- Zhai, Y. et al. Giant Rashba splitting in 2D organic-inorganic halide perovskites measured by transient spectroscopies. Sci. Adv. 3, e1700704 (2017).

- Ni, Z. et al. Resolving spatial and energetic distributions of trap states in metal halide perovskite solar cells. Science 367, 1352–1358 (2020).
- 8. Steirer, K. X. et al. Defect tolerance in methylammonium lead triiodide perovskite. ACS Energy Lett. 1, 360–366 (2016).
- Lin, K. et al. Perovskite light-emitting diodes with external quantum efficiency exceeding 20 per cent. *Nature* 562, 245–248 (2018).
- Wang, Y. et al. Thermodynamically stabilized β-CsPbI<sub>3</sub>-based perovskite solar cells with efficiencies >18%. Science 365, 591–595 (2019).
- Zhu, X. Y. & Podzorov, V. Charge carriers in hybrid organicinorganic lead halide perovskites might be protected as large polarons. J. Phys. Chem. Lett. 6, 4758–4761 (2015).
- Zheng, F. & Wang, L. Large polaron formation and its effect on electron transport in hybrid perovskites. *Energy Environ*. Sci. 12, 1219–1230 (2019).
- 13. Miyata, K., Atallah, T. L. & Zhu, X.-Y. Lead halide perovskites: crystal-liquid duality, phonon glass electron crystals, and large polaron formation. Sci. Adv. 3, e1701469 (2017).
- Puppin, M. et al. Evidence of large polarons in photoemission band mapping of the perovskite semiconductor CsPbBr<sub>3</sub>. Phys. Rev. Lett. 124, 206402 (2020).
- Guzelturk, B. et al. Visualization of dynamic polaronic strain fields in hybrid lead halide perovskites. *Nat. Mater.* 20, 618–623 (2021)
- Frost, J. M. et al. Atomistic origins of high-performance in hybrid halide perovskite solar cells. *Nano Lett.* 14, 2584–2590 (2014).
- Frost, J. M., Butler, K. T. & Walsh, A. Molecular ferroelectric contributions to anomalous hysteresis in hybrid perovskite solar cells. APL Mater. 2, 081506 (2014).
- Liu, S. et al. Ferroelectric domain wall induced band gap reduction and charge separation in organometal halide perovskites. J. Phys. Chem. Lett. 6, 693–699 (2015).
- Strelcov, E. et al. CH<sub>3</sub>NH<sub>3</sub>PbI<sub>3</sub> perovskites: ferroelasticity revealed. Sci. Adv. 3, e1602165 (2017).
- 20. Hoque, M. N. F. et al. Polarization and dielectric study of methylammonium lead iodide thin film to reveal its nonferroelectric nature under solar cell operating conditions. ACS Energy Lett. 1, 142–149 (2016).
- 21. Liu, Y. et al. Chemical nature of ferroelastic twin domains in CH<sub>3</sub>NH<sub>3</sub>Pbl<sub>3</sub> perovskite. *Nat. Mater.* **17**, 1013–1019 (2018).
- Schulz, A. D. et al. On the ferroelectricity of CH<sub>3</sub>NH<sub>3</sub>PbI<sub>3</sub> perovskites. *Nat. Mater.* 18, 1050 (2019).
- Miyata, K. & Zhu, X.-Y. Ferroelectric large polarons. *Nat. Mater.* 17, 379–381 (2018).
- 24. Wang, F. et al. Solvated electrons in solids—ferroelectric large polarons in lead halide perovskites. *J. Am. Chem.* Soc. **143**, 5–16 (2021).
- 25. Huang, H. Ferroelectric photovoltaics. *Nat. Photon.* **4**, 134–135 (2010).
- Morris, M. R., Pendlebury, S. R., Hong, J., Dunn, S. & Durrant, J. R. Effect of internal electric fields on charge carrier dynamics in a ferroelectric material for solar energy conversion. *Adv. Mater.* 28, 7123–7128 (2016).
- 27. Liu, Y. et al. Approaching the Schottky–Mott limit in van der Waals metal–semiconductor junctions. *Nature* **557**, 696–700 (2018).
- Zhang, J., Li, C., Chen, M. & Huang, K. Real-time observation of ion migration in halide perovskite by photoluminescence imaging microscopy. J. Phys. D 54, 044002 (2021).
- Zhang, T. et al. Understanding the relationship between ion migration and the anomalous hysteresis in high-efficiency perovskite solar cells: a fresh perspective from halide substitution. Nano Energy 26, 620–630 (2016).

- Zhong, Y., Hufnagel, M., Thelakkat, M., Li, C. & Huettner, S. Role of PCBM in the suppression of hysteresis in perovskite solar cells. Adv. Funct. Mater. 30, 1908920 (2020).
- 31. Chen, Q. et al. All-inorganic perovskite nanocrystal scintillators. *Nature* **561**, 88–93 (2018).
- Tsai, H. et al. A sensitive and robust thin-film X-ray detector using 2D-layered perovskite diodes. Sci. Adv. 6, eaay0815 (2020).
- 33. Miyata, K. et al. Large polarons in lead halide perovskites. *Sci. Adv.* **3**, e1701217 (2017).
- Park, M. et al. Excited-state vibrational dynamics toward the polaron in methylammonium lead iodide perovskite. *Nat. Commun.* 9, 2525 (2018).
- Oga, H., Saeki, A., Ogomi, Y., Hayase, S. & Seki, S. Improved understanding of the electronic and energetic landscapes of perovskite solar cells: high local charge carrier mobility, reduced recombination, and extremely shallow traps. *J. Am. Chem.* Soc. 136, 13818–13825 (2014).
- 36. Eperon, G. E. et al. Formamidinium lead trihalide: a broadly tunable perovskite for efficient planar heterojunction solar cells. *Energy Environ. Sci.* **7**, 982–988 (2014).
- Schlaus, A. P. et al. How lasing happens in CsPbBr<sub>3</sub> perovskite nanowires. Nat. Commun. 10, 265 (2019).
- Miyata, K. et al. Liquid-like dielectric response is an origin of long polaron lifetime exceeding 10 μs in lead bromide perovskites.
  J. Chem. Phys. 152, 084704 (2020).
- Abdelkefi, H., Khemakhem, H., Vélu, G., Carru, J. C. & Von der Mühll, R. Dielectric properties and ferroelectric phase transitions in Ba<sub>x</sub>Sr<sub>1-x</sub>TiO<sub>3</sub> solid solution. *J. Alloys Compd* 399, 1–6 (2005).
- 40. Onoda-Yamamuro, N., Matsuo, T. & Suga, H. Dielectric study of CH<sub>3</sub>NH<sub>3</sub>PbX<sub>3</sub> (X=Cl, Br, I). *J. Phys. Chem. Solids* **53**, 935–939 (1992).
- Wilson, J. N., Frost, J. M., Wallace, S. K. & Walsh, A. Dielectric and ferroic properties of metal halide perovskites. APL Mater. 7, 010901 (2019).

- 42. Viehland, D., Jang, S. J., Cross, L. E. & Wuttig, M. Freezing of the polarization fluctuations in lead magnesium niobate relaxors. *J. Appl. Phys.* **68**, 2916–2921 (1990).
- Glazounov, A. E. & Tagantsev, A. K. Direct evidence for Vögel– Fulcher freezing in relaxor ferroelectrics. Appl. Phys. Lett. 73, 856–858 (1998).
- 44. Viehland, D., Li, J. F., Jang, S. J., Cross, L. E. & Wuttig, M. Dipolar-glass model for lead magnesium niobate. *Phys. Rev. B* **43**, 8316–8320 (1991).
- Westphal, V., Kleemann, W. & Glinchuk, M. D. Diffuse phase transitions and random-field-induced domain states of the 'relaxor' ferroelectric PbMg<sub>1/3</sub>Nb<sub>2/3</sub>O<sub>3</sub>. Phys. Rev. Lett. 68, 847–850 (1992).
- 46. Krogstad, M. J. et al. The relation of local order to material properties in relaxor ferroelectrics. *Nat. Mater.* **17**, 718–724 (2018).
- 47. Kumar, A. et al. Atomic-resolution electron microscopy of nanoscale local structure in lead-based relaxor ferroelectrics. *Nat. Mater.* **20**, 62–67 (2021).
- 48. Liu, Y. et al. Chirality-induced relaxor properties in ferroelectric polymers. *Nat. Mater.* **19**, 1169–1174 (2020).
- 49. Li, W., She, Y., Vasenko, A. S. & Prezhdo, O. V. Ab initio nonadiabatic molecular dynamics of charge carriers in metal halide perovskites. *Nanoscale* **13**, 10239–10265 (2021).

**Publisher's note** Springer Nature remains neutral with regard to jurisdictional claims in published maps and institutional affiliations.

Springer Nature or its licensor (e.g. a society or other partner) holds exclusive rights to this article under a publishing agreement with the author(s) or other rightsholder(s); author self-archiving of the accepted manuscript version of this article is solely governed by the terms of such publishing agreement and applicable law.

@ The Author(s), under exclusive licence to Springer Nature Limited 2023

#### Methods

#### Material growth

The precursors CsBr and PbBr $_2$  at a molar ratio of 1:1 were mixed together well. The mixture was heated to 380 °C for 12 h to form the CsPbBr $_3$  powder, which was used for growth of the CsPbBr $_3$  thin film using a home-built tube furnace system (Lindberg/Blue M, Thermo Scientific) via a vapour phase deposition process under a controlled pressure. The CsPbBr $_3$  powder source was placed at the centre of the furnace in a quartz tube (2.5 cm diameter), and the exfoliated muscovite with a freshly exposed surface was placed downstream as the growth substrate. The system was pumped down and flushed with argon gas three times before being stabilized at 190 mbar with 100 sccm argon as the carrier gas. The furnace was ramped to 530 °C and kept at this temperature for 1 h for the preparation of a CsPbBr $_3$  thin film with a thickness of 1  $\mu$ m.

#### **Device fabrication**

For the vertical device, the CsPbBr<sub>3</sub> perovskite thin film was first peeled off from the muscovite substrate, using thermal release tape, and then dry transferred on to a prefabricated 50-nm-thick Au electrode on a sapphire substrate. It was then heated to 90 °C to release the thermal tape. The top Au electrode was prepared following a van der Waals contacting approach. For this, 50-nm-thick Au electrodes were first prepared on a silicon substrate using standard photolithography. Next, a hexamethyldisilazane layer was applied to functionalize the whole wafer and then a poly(methyl methacrylate) (PMMA) layer was spin-coated on top of the Au electrodes. With the pre-functionalization of hexamethyldisilazane, the PMMA layer had weak adhesion to the sacrificial substrate and could be mechanically picked up using the thermal release tape, together with the metal electrodes embedded underneath. The thermal release tape with the electrodes was laminated to the film directly and heated to 90 °C to release the PMMA layer. Electron-beam lithography was applied to make windows in the PMMA layer, exposing the embedded electrode pads for subsequent electrical measurements. This van der Waals contacting approach was also adapted to prepare the lateral Hall bar device, with the mesa isolation accomplished via mechanical scratching. The Hall bar channel length was 1 mm.

#### **Device characterization**

Device characterization was carried out using a commercial PPMS measurement system (Quantum Design). The illumination source was a blue light-emitting diode (464 nm) installed on the chip carrier. The power density of the illumination was determined using a power meter (1916-R, Newport Optical) with measurement head (818-SL, Newport Optical). The electrical measurements were carried out using an LCR meter (4263B, Agilent) for the conductance measurements, a precision source/measure unit (B2902A, Agilent) for direct-current measurements and a lock-in amplifier (SR830) connected in series with a current pre-amplifier (DL1201) for low-frequency alternating-current measurements. The excitation voltage for the persistence photoconductance measurements was 0.1V.

## Fitting of photoconductance decay

We obtained the polaron-assisted carrier lifetime  $\tau$  using the following equation:

$$G(t) = G_{\text{light}} \left[ A_1 \exp(-t/\tau_1) + A_2 \exp(-t/\tau_2) + A_3 \exp(-t/\tau_3) \right] + G_{\text{dark}}$$
 (2)

where  $G_{\text{light}}$  is the conductance under illumination and  $G_{\text{dark}}$  is the conductance in the dark;  $A_1$ ,  $A_2$ ,  $A_3$  and  $\tau_1$ ,  $\tau_2$ ,  $\tau_3$  are fitting parameters. Lifetime parameter  $\tau_1$  (-3.7 s) is the fastest component involving free carrier recombination but is limited by the instrument response

function in our measurements;  $\tau_2$  is the trap-related lifetime; and  $\tau_3$  corresponds to the slowest decay rate, which is the persistent photocarrier lifetime  $\tau$  discussed in Fig. 2 of the main text, and is related to the ferroelectric large polaron recombination that is the focus of this study. For the data at 10 K shown in Fig. 2,  $\tau_1$  is 3.7 s,  $\tau_2$  is  $3 \times 10^2$  s and  $\tau_3$  is  $1 \times 10^6$  s. The overall amplitude of the photoconductance decay is dominated by  $A_1$  (80.1%) and  $A_3$  (19.5%), and  $A_2$  contributes only 0.4%.

#### X-ray diffraction experiments

We carried out X-ray diffraction studies using a Panalytical X'Pert Pro X-ray powder diffractometer, with the sample loaded in a Phenix cryostage for cooling purpose. The photocarrier generation rate Q (cm<sup>-3</sup> s<sup>-1</sup>) is related to the X-ray incident photon flux G (cm<sup>-2</sup> s<sup>-1</sup>) through the following relationship:

$$Q = \frac{\text{energy absorption rate}}{\text{ionization energy}} = \frac{G \times \varepsilon \times \gamma}{l \times W}$$
 (3)

where  $\varepsilon$  is the X-ray photon energy, W is the ionization energy and  $\gamma$  is the absorption efficiency. Here,  $\gamma=1-\exp(-\eta d)$ , where  $\eta$  is the linear absorption coefficient and d is the absorption thickness, which is equal to the material thickness ( $l=1\,\mu m$ ) divided by  $\sin\theta$ , where  $\theta$  is the X-ray diffraction angle. In our study, we measured G directly, with G tuned by changing the X-ray operation power; in addition, we used W and  $\eta$  reported for CH<sub>3</sub>NH<sub>3</sub>PbI<sub>3</sub> in ref. <sup>32</sup> and estimated the carrier density based on its relationship with Q shown in ref. <sup>4</sup>. In our experiments, we used an X-ray power density of  $0.04-1.2\,\mu W$  cm<sup>-2</sup>, which produces a carrier density of  $-10^{14}-10^{15}$  cm<sup>-3</sup> and overlaps with the lower end of our photoconductance studies ( $-10^{14}-10^{16}$  cm<sup>-3</sup>) under visible-light excitation.

#### **Computational details**

We performed spin-polarized DFT calculations within the Perdew-Burke-Ernzerhof exchange functional<sup>50</sup> of the open source plane-wave QUANTUM ESPRESSO package<sup>51</sup>. We used the GBRV ultrasoft potentials<sup>52</sup> with an energy cut-off for a wavefunction of 40 Ry and an energy cut-off for a charge density of 240 Ry. We first optimized the lattice constant in five-atom pristine cubic CsPbBr<sub>3</sub> and obtained a = b = c = 6.002 Å. Using the relaxed lattice parameters, we extended the supercell size as needed. For supercell calculations, we relaxed only the atomic positions until all atomic forces were smaller than 1 mRy bohr<sup>-1</sup> using a  $1 \times 1 \times 2$  and  $2 \times 2 \times 1$   $\Gamma$ -centred k-grid for the  $8 \times 8 \times 2$  and  $2 \times 2 \times 8$  supercell, respectively. To evaluate the local polarization P, we used P = qd/V, where q is the Born effective charge  $^{\rm 53}$  for Pb, d is the displacement from the centre of charge by the six Br octahedra and V is the volume of the octahedra. The maximum local polarization in the  $2 \times 2 \times 8$  supercell in Fig. 5e is 20 μC cm<sup>-2</sup>. In this Article, we assigned the high polar, intermediate polar and small polar regions as  $|P| \ge 10, 10 > |P| \ge 5$  and  $|P| < 5 (\mu \text{C cm}^{-2})$ , respectively.

#### **Data availability**

The data that support the plots within this paper and other findings of this study are available from the corresponding authors upon reasonable request.

# **Code availability**

The custom codes that support the findings of this study are available from the corresponding authors upon reasonable request.

#### References

 Perdew, J. P., Burke, K. & Ernzerhof, M. Generalized gradient approximation made simple. *Phys. Rev. Lett.* 77, 3865–3868 (1996).

- Giannozzi, P. et al. QUANTUM ESPRESSO: a modular and open-source software project for quantum simulations of materials. J. Phys. Condens. Matter 21, 395502 (2009).
- Garrity, K. F., Bennett, J. W., Rabe, K. M. & Vanderbilt, D. Pseudopotentials for high-throughput DFT calculations. Comput. Mater. Sci. 81, 446–452 (2014).
- Kang, B. & Biswas, K. Exploring polaronic, excitonic structures and luminescence in Cs<sub>4</sub>PbBr<sub>6</sub>/CsPbBr<sub>3</sub>. J. Phys. Chem. Lett. 9, 830–836 (2018).

# **Acknowledgements**

X.D. acknowledges partial support by the Office of Naval Research through grant no. NO0014-22-1-2631 for device fabrication and characterization, Y.P. acknowledges support by the Center for Hybrid Organic Inorganic Semiconductors for Energy an Energy Frontier Research Center funded by the Office of Basic Energy Sciences, office of science within the US Department of Energy for the theoretical part of the work. T.J.S. acknowledges the Lawrence Livermore National Laboratory Graduate Research Scholar Program and funding support from Lawrence Livermore National Laboratory LDRD 20-S1-004. Part of this work was performed under the auspices of the US Department of Energy by the Lawrence Livermore National Laboratory under Contract DE-AC52-07NA27344. The X-ray diffraction measurements used the resources of the Center for Nanophase Materials Sciences and Spallation Neutron Source, which are DOE Office of Science User Facilities. Y.H. acknowledges support by the National Science Foundation EFRI-1433541 for partial support of material preparation. We acknowledge the Nanoelectronics Research Facility at UCLA for device fabrication technical support.

#### **Author contributions**

X.D. conceived the research. Q.Q., Z.W. and X.D. designed the experiments. Q.Q. grew the material, fabricated the devices and performed the optoelectrical measurements. L.W., P.W., D.X. and Y.H. contributed to the device fabrication or characterization. Z.W. contributed to the transport measurements. J.K.K., J.Z. and H.R. contributed to the X-ray diffraction experiments. H.T., T.J.S. and Y.P. conducted the first-principles calculations and wrote the relevant discussions. Q.Q., Z.W. and X.D. conducted the data analysis and wrote the paper. All authors discussed the results and commented on the manuscript.

## **Competing interests**

The authors declare no competing interests.

#### **Additional information**

**Supplementary information** The online version contains supplementary material available at https://doi.org/10.1038/s41565-022-01306-x.

**Correspondence and requests for materials** should be addressed to Yuan Ping or Xiangfeng Duan.

**Peer review information** *Nature Nanotechnology* thanks Doru Lupascu and Kiyoshi Miyata for their contribution to the peer review of this work.

**Reprints and permissions information** is available at www.nature.com/reprints.